



ELSEVIER

Available online at www.sciencedirect.com

 ScienceDirect

Journal of Crystal Growth 297 (2006) 20–32

JOURNAL OF **CRYSTAL GROWTH**

www.elsevier.com/locate/jcrysgro

Transient numerical study of temperature gradients during sublimation growth of SiC: Dependence on apparatus design

Jürgen Geiser^a, Olaf Klein^b, Peter Philip^{b,*}

^a*Humboldt-Universität zu Berlin, Department of Mathematics, Unter den Linden 6, 10099 Berlin, Germany*

^b*Weierstrass Institute for Applied Analysis and Stochastics (WIAS), Mohrenstraße 39, 10117 Berlin, Germany*

Received 18 November 2005; received in revised form 5 May 2006; accepted 28 August 2006

Communicated by M.E. Glicksman

Available online 27 October 2006

Abstract

Using transient and stationary mathematical heat transfer models including heat conduction, radiation, and radio frequency (RF) induction heating, we numerically investigate the time evolution of temperature gradients in axisymmetric growth apparatus during the sublimation growth of silicon carbide (SiC) bulk single crystals by physical vapor transport (PVT) (modified Lely method). Temperature gradients in the bulk and on the surface of the growing crystal can cause defects. Here, the evolution of these gradients is studied numerically during the heating, growth, and cooling stages, varying the apparatus design, namely the amount of the source powder charge as well as the size of the upper blind hole used for cooling of the seed. Our results show that a smaller upper blind hole can reduce the temperature gradients both in the bulk and on the surface of the crystal without reducing the surface temperature itself.

© 2006 Elsevier B.V. All rights reserved.

PACS: 02.60.Cb; 81.10.Bk; 44.05.+e; 47.27.Te

Keywords: A1. Computer simulation; A1. Heat transfer; A2. Growth from vapor; A2. Single crystal growth; B2. Semiconducting silicon compounds

1. Introduction

Silicon carbide (SiC) is a wide-bandgap semiconductor used in high-power and high-frequency industrial applications: SiC serves as substrate material for electronic and optoelectronic devices such as MOSFETs, thyristors, blue lasers, and sensors (see Ref. [1] for a recent account of advances in SiC devices). Its chemical and thermal stability make SiC an attractive material to be used in high-temperature applications as well as in intensive-radiation environments. For an economically viable industrial use of SiC, growth techniques for large-diameter, low-defect SiC boules must be available. Recent years have seen steady improvement (see Ref. [2]) of size and quality of SiC single crystals grown by sublimation via *physical vapor transport* (PVT, also known as the modified Lely method, see e.g.

Refs. [3,4]). However, many problems remain, warranting further research.

Typically, modern PVT growth systems consist of an induction-heated graphite crucible containing polycrystalline SiC source powder and a single-crystalline SiC seed (see Fig. 1). The source powder is placed in the hot zone of the growth apparatus, whereas the seed crystal is cooled by means of a blind hole, establishing a temperature difference between source and seed. As the SiC source is kept at a higher temperature than the cooled SiC seed, sublimation is encouraged at the source and crystallization is encouraged at the seed, causing the partial pressures of Si, Si₂C, and SiC₂ to be higher in the neighborhood of the source and lower in the neighborhood of the seed. As the system tries to equalize the partial pressures, source material is transported to the seed which grows into the reaction chamber.

Controlling the temperature distribution in the growth apparatus is essential for achieving a low-defect growth of large SiC bulk single crystals. Temperature gradients and

*Corresponding author. Tel.: +49 30 20372 531; fax: +49 30 2044 975.
E-mail address: philip@wias-berlin.de (P. Philip).

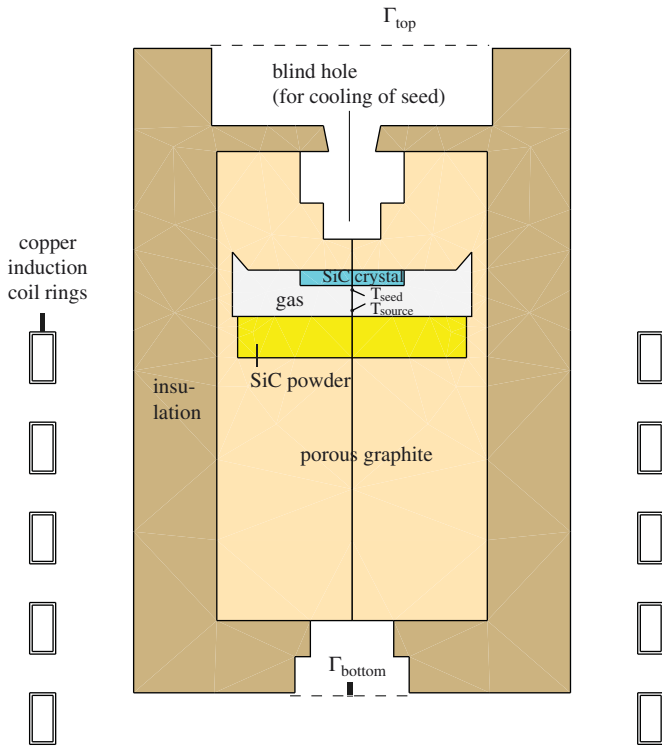


Fig. 1. Setup of growth apparatus according to Ref. [5, Fig. 2].

resulting thermal stresses in the SiC single crystal can cause defects. Large temperature gradients in the bulk of the crystal must therefore be avoided during all stages of the process (heating, growth, cooling). Moreover, temperature gradients on the growing crystal's surface can lead to defects being built into the crystal during growth, where experimental evidence shows that growth on the seed crystal can already occur during the heating phase [6]. For experimental studies supporting the described relationships between temperature gradients and defects in the as-grown crystal see, e.g., Refs. [7–9]. However, owing to the high temperatures, experimental verification of the correlation between the design of the growth apparatus and the temperature distribution inside the growth chamber is extremely difficult and costly. In consequence, the development of numerical models and software and their application to PVT growth of SiC crystals has been an active field of research in recent years, see, e.g., Refs. [10–14] and references therein. While temperature fields in SiC growth systems and their dependence on PVT apparatus design have been the subject of many, both transient and stationary, numerical studies (including the above-quoted papers), the authors are not aware of a transient numerical investigation of the temperature gradient evolution including the heating and cooling stages, even though, as described, reducing temperature gradients during both heating and cooling as well as at growth temperature is conducive to reducing crystal defects. It is the goal of the present paper to numerically simulate the evolution of the temperature field during the

heating phase, at growth temperature, and during the cooling phase, assessing how varying the size of the upper blind hole and the size of the source powder charge can be used to reduce the temperature gradients.

The paper is organized as follows: In Section 2, we describe the mathematical model for the heat transfer and for the induction heating. The employed numerical methods and the implementation tools are covered in Section 3. We present our numerical experiments in Section 4, where the general setting is detailed in Section 4.1, and numerical results analyzing the effect of the size of the upper blind hole as well as the amount of the source powder on the evolution of the temperature gradients in the bulk and on the surface of the SiC seed crystal are reported on and discussed in Section 4.2.

2. Modeling of heat transfer and induction heating

The numerical results of Section 4 below are based on our previously published model of transient and stationary heat transport in induction-heated PVT growth systems (see Refs. [12,15] and references therein). For the convenience of the reader, we briefly recall the scope and assumptions of the model as well as the main governing equations, interface, and boundary conditions. The heat transport model includes conduction through solid materials as well as through the gas phase as described, for the transient case, by the heat equations

$$\rho_m \partial_t e_m + \text{div } \vec{q}_m = f_m, \quad (1a)$$

$$\vec{q}_m = -\kappa_m(T) \nabla T \quad \text{in } \Omega_m, \quad (1b)$$

where the index m refers to a material that can be either the gas phase or a solid component of the growth apparatus, ρ_m denotes mass density, t denotes time, e_m denotes internal energy, \vec{q}_m denotes heat flux, f_m denotes power density (per volume) caused in conducting materials due to induction heating, κ_m denotes thermal conductivity, T denotes absolute temperature, and Ω_m is the domain of material m . The stationary heat transport model is analogous, merely without the time-dependent term in Eq. (1a). The transient model was used to compute the time-dependent temperature fields during the heating and cooling processes. The stationary model was used to compute temperature fields at growth temperature for different lengths of the SiC seed crystal as detailed in Section 4.2. During both heating and cooling, the temperature field is far from equilibrium, such that the use of the transient model is essential. However, once the field has reached a quasi-equilibrium, subsequent changes are mainly due to the increasing length of the crystal and the decreasing height of the source powder. The rate of these changes is in the order of mm/h. Due to this slow change, the use of the stationary model seems justified, especially, as the use of the transient model during this stage would mean frequent remeshing and recalculation of view factors (cf. Section 3).

It is assumed that the gas phase is made up solely of argon, which is a reasonable assumption for simulations of the temperature distribution [16, Section 5]. Then, the internal energy in the gas phase takes the form

$$e_{\text{gas}}(T) = 3RT/(2M_{\text{Ar}}), \quad (2a)$$

R denoting the gas constant and M_{Ar} denoting the molecular mass of argon. The internal energy of the solid material m_i is given by

$$e_{m_i}(T) = \int_{T_0}^T c_{m_i}(S) dS, \quad (2b)$$

where c_{m_i} denotes specific heat and T_0 is a reference temperature. The temperature is assumed to be continuous throughout the apparatus. To formulate the interface conditions for the heat flux, let β and β' denote different solid components of the growth apparatus. The normal heat flux is assumed to be continuous on an interface $\gamma_{\beta,\beta'}$ between two solid opaque materials β and β' , i.e. the interface condition is given by Eq. (3a). If the solid material β is the semi-transparent SiC single crystal or on an interface $\gamma_{\beta',\text{gas}}$ between the solid material β' and the gas phase, one needs to account for radiosity R and for irradiation J , resulting in interface conditions (3b) and (3c), respectively.

$$\vec{q}^{[\beta]} \cdot \vec{n}^{[\beta]} = \vec{q}^{[\beta']} \cdot \vec{n}^{[\beta]} \quad \text{on } \gamma_{\beta,\beta'}, \quad (3a)$$

$$\vec{q}^{[\beta]} \cdot \vec{n}^{[\beta]} - R + J = \vec{q}^{[\beta']} \cdot \vec{n}^{[\beta]} \quad \text{on } \gamma_{\beta,\beta'}, \quad (3b)$$

$$\vec{q}_{\text{gas}} \cdot \vec{n}_{\text{gas}} - R + J = \vec{q}^{[\beta]} \cdot \vec{n}_{\text{gas}} \quad \text{on } \gamma_{\beta,\text{gas}}, \quad (3c)$$

where $\vec{n}^{[\beta]}$ is the outer unit normal vector to the solid material β , and \vec{n}_{gas} is the outer unit normal vector to the gas phase. The radiative quantities R and J are modeled using the net radiation method for diffuse-gray radiation as described in Ref. [12, Section 2.5], where a band approximation model is used to account for the semi-transparency of the SiC single crystal. The growth apparatus is considered in a black body environment (e.g. a large isothermal room) radiating at room temperature T_{room} , such that outer boundaries emit according to the Stefan–Boltzmann law:

$$\vec{q}^{[\beta]} \cdot \vec{n}^{[\beta]} = \sigma \varepsilon^{[\beta]} (T^4 - T_{\text{room}}^4), \quad (4)$$

where $\sigma = 5.6696 \times 10^{-8} \text{ W/m}^2 \text{ K}^4$ denotes the Boltzmann radiation constant, and $\varepsilon^{[\beta]}$ denotes the (temperature-dependent) emissivity of the surface. On outer boundaries receiving radiation from other parts of the apparatus, i.e. on the surfaces of the upper and lower blind hole, the situation is more complicated. On such boundaries, as in Eqs. (3b) and (3c), one has to account for radiosity R and irradiation J , leading to the boundary condition

$$\vec{q}^{[\beta]} \cdot \vec{n}^{[\beta]} - R + J = 0, \quad (5)$$

where, as before, the modeling of R and J is as described in Ref. [12, Section 2.5]. For the two blind holes, we use black body phantom closures (denoted by Γ_{top} and Γ_{bottom} in

Fig. 1) which emit radiation at T_{room} . We thereby allow for radiative interactions between the open cavities and the ambient environment, including reflections at the cavity surfaces.

Induction heating causes eddy currents in the conducting materials of the growth apparatus, resulting in the heat sources f_m of Eq. (1a) due to the Joule effect. Assuming axisymmetry of all components of the growth system as well as of all relevant physical quantities, and, furthermore, assuming sinusoidal time dependence of the imposed alternating voltage, the heat sources are computed via an axisymmetric complex-valued magnetic scalar potential that is determined as the solution of an elliptic partial differential equation (see Ref. [12, Section 2.6]). To prescribe the total heating power, we follow Ref. [17, Section II], ensuring that the total current is the same in each coil ring. The distribution of the heat sources is redetermined in each time step of the transient problem for the temperature evolution to account for temperature dependence of the electrical conductivity.

All simulations presented in this article are performed for an idealized growth apparatus, treating all solid materials as homogeneous and pure, neglecting effects such as the sintering of the SiC source powder, changes in the porosity of the graphite, and Si accumulation in the insulation.

3. Numerical methods and implementation

For the numerical computations presented in Section 4.2, i.e. for the stationary simulations of the magnetic scalar potential as well as for the transient and stationary temperature simulations, a finite volume method is used for the spatial discretizations of the nonlinear partial differential equations that arise from the model described in Section 2. An implicit Euler scheme provides the time discretization of the temperature evolution equation; only emissivity terms are evaluated explicitly, i.e. using the temperature at the previous time step. The used scheme, including the discretization of nonlocal terms stemming from the modeling of diffuse-gray radiation, was previously described in Refs. [15,18]. The convergence of the scheme has been verified numerically for stationary cases in Refs. [19,20].

The finite volume discretization of the nonlocal radiation terms involves the calculation of visibility and view factors. The method used is based on Ref. [21] and is described in Ref. [16, Section 4].

The discrete scheme was implemented as part of our software *WIAS-HiTNIHS*¹ which is based on the program package *pdelib* [22]. In particular, *pdelib* uses the grid generator *Triangle* [23] to produce constrained Delaunay triangulations of the domains, and it uses the sparse matrix solver *PARDISO* [24,25] to solve the linear system arising

¹High Temperature Numerical Induction Heating Simulator; pronunciation: ~hit-nice.

from the linearization of the finite volume scheme via Newton’s method.

4. Numerical experiments

4.1. General setting

All numerical simulations presented in the following were performed for the growth system [5, Fig. 2] displayed in Fig. 1, consisting of a container having a radius of 8.4 cm and a height of 25 cm placed inside of five hollow rectangular-shaped copper induction rings. Using cylindrical coordinates (r, z) , the upper rim of the induction coil is located at $z = 14$ cm, and its lower rim is located at $z = -2.0$ cm, i.e. 2 cm lower than the lower rim of the rest of the apparatus (see Fig. 1). The geometric proportions of the coil rings are provided in Fig. 2.

The material data used for the following numerical experiments are precisely the data provided in the appendices of Refs. [16,26,27], respectively. The angular frequency used for the induction heating is $\omega = 2\pi f$, where $f = 10$ kHz.

4.2. Transient numerical investigation of the temperature gradients

We conduct four series of numerical experiments, referred to as Experiments (a)–(d) in the following, varying the amount of the source powder and the size of the upper blind hole as will be explained in detail below. Each series consists of two transient and five stationary simulations of the temperature field in the growth apparatus: a transient simulation of the heating phase; five stationary simulations of the growth stage, where the length of the crystal is increased successively; and a transient simulation of the cooling phase.

Each transient simulation of the heating phase starts at $T_{\text{room}} = 293$ K. The average total power P is prescribed according to the following linear ramp:

$$P(t) := \begin{cases} P_{\min} & \text{for } t \leq t_0, \\ P_{\min} + \frac{(t - t_0)(P_{\max} - P_{\min})}{t_1 - t_0} & \text{for } t_0 \leq t \leq t_1, \\ P_{\max} & \text{for } t_1 \leq t, \end{cases} \quad (6)$$

where $t_0 = 0.5$ h, $t_1 = 3.0$ h, $P_{\min} = 2$ kW, and $P_{\max} = 7$ kW. The same value for P_{\max} is then used for each of the five stationary simulations, which we denote by $\Delta l_c = 0, 2.5, 5, 7.5,$ and 10 mm, where Δl_c is the amount of crystal length that is assumed to be added during the growth phase. At a growth rate of 1 mm/h, the five stationary simulations cover 10 h of growth. As SiC is added to the seed crystal, the amount of source powder is reduced. In a rough approximation, we assume that the mass of SiC added to the crystal equals the mass of SiC by which the source is diminished. Also assuming that the height of the source is reduced homogeneously by Δl_p ,

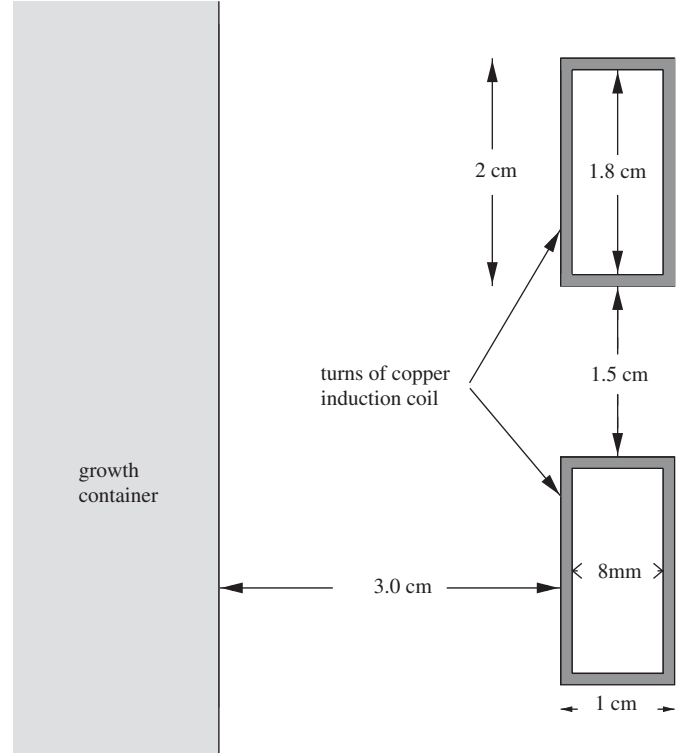


Fig. 2. Geometric proportions of induction coil rings.

using the mass densities $\rho_c = 3140$ kg/m³ and $\rho_p = 1700$ kg/m³ for SiC crystal and source, respectively (see Ref. [16]), as well as taking into account axisymmetry, one obtains $\Delta l_p = 0.4 \Delta l_c$. The changes in crystal length and powder height are depicted in the columns of Fig. 3. In practice, material is exchanged between the SiC source and the crucible walls, chemical reactions and phase transitions result in density changes in the source and Δl_p depends on the radial coordinate. However, accounting for these effects is beyond the scope of this article. The transient simulations of the cooling stage use the result of the corresponding stationary simulation with $\Delta l_c = 10$ mm as initial condition. Here, the linearly decreasing average total power P is prescribed according to

$$P(t) := \begin{cases} P_{\max} - \frac{tP_{\max}}{t_2} & \text{for } 0 \leq t \leq t_2, \\ 0 & \text{for } t_2 \leq t, \end{cases} \quad (7)$$

where $t_2 = 2.5$ h and $P_{\max} = 7$ kW.

As stated above, all three stages (heating, growth phase, cooling) are simulated in each of the four numerical experiments (a)–(d), varying the amount of the source powder and the size of the upper blind hole: we consider two different amounts of source powder, where the larger amount is 5 times the smaller amount. We employ the abbreviations powder = 1 and powder = 5 to indicate the use of the small and large amount of source powder, respectively. We consider two different sizes for the upper blind hole, the situation with the smaller hole being

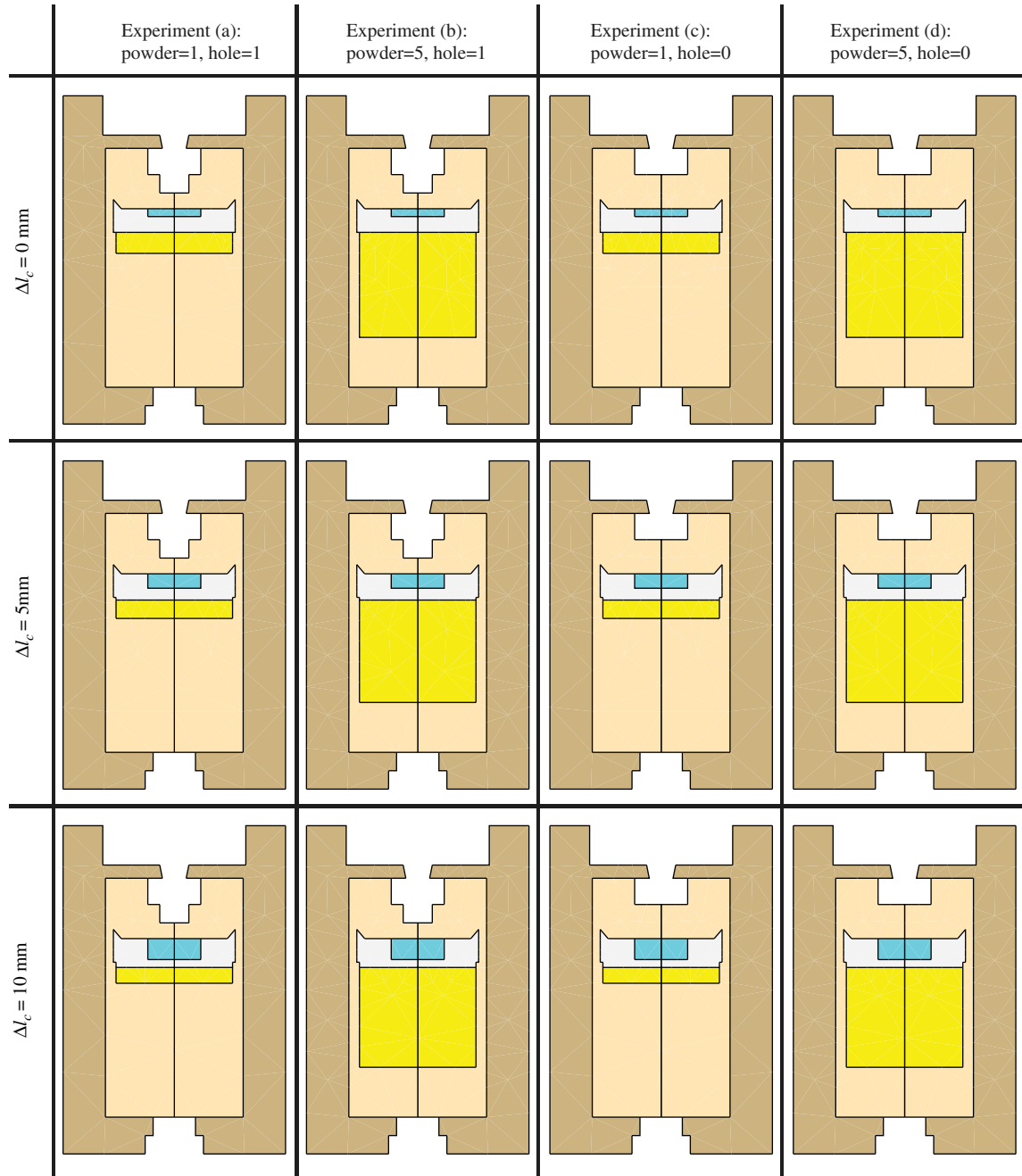


Fig. 3. Apparatus designs for Experiments (a)–(d), where Δl_c denotes the change in crystal length during the growth phase. Here, it is also assumed that the powder height decreases by $\Delta l_p = 0.4 \Delta l_c$ (cf. discussion in Section 4.2).

referred to as hole = 0, and the situation with the larger hole being referred to as hole = 1. The resulting different apparatus designs used in the four experiments are depicted in Fig. 3: we use powder = 1, hole = 1 in Experiment (a); powder = 5, hole = 1 in Experiment (b); powder = 1, hole = 0 in Experiment (c); and powder = 5, hole = 0 in Experiment (d).

As described earlier, controlling the temperature gradient in the bulk and on the surface of the SiC single crystal is of particular importance in order to avoid crystal defects in the as-grown crystal, where large temperature gradients in

the bulk must be avoided throughout heating, growth, and cooling, while the temperature on the seed's surface should be as homogeneous as possible once growth has been initiated. In each of the considered apparatus designs, the domain of the SiC seed crystal is the set

$$\Omega_{\text{seed}} := \{(r, \theta, z) : 0 \leq r \leq 2 \text{ cm}, 15.8 \text{ cm} - \Delta l_c \leq z \leq 16.4 \text{ cm}\}, \quad (8)$$

and the seed's surface is the set

$$\Sigma := \{(r, \theta, z) : 0 \leq r \leq 2 \text{ cm}, z = 15.8 \text{ cm} - \Delta l_c\}, \quad (9)$$

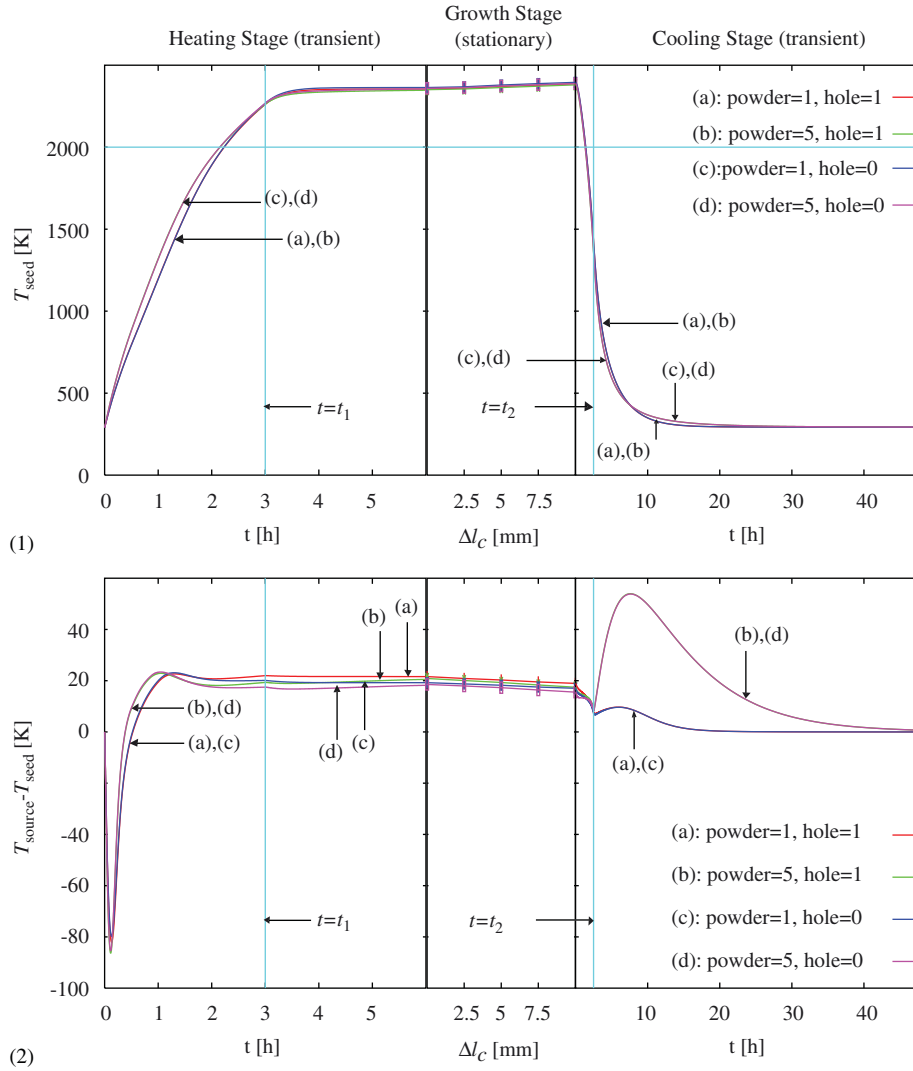


Fig. 4. Evolution of T_{seed} and of $T_{source} - T_{seed}$ for Experiments (a)–(d), where T_{seed} is the temperature at $(r, z) = (0, 15.8 \text{ cm} - \Delta l_c)$ and T_{source} is the temperature at $(r, z) = (0, 14.6 \text{ cm})$ (cf. Fig. 1). Results of transient simulations for heating and cooling stages, results of 5 stationary simulations (linearly interpolated) for each experiment for the growth stage.

where, here and in the following, (r, θ, z) denote cylindrical coordinates. The temperature where growth is initiated depends on the SiC polytype to be grown, but growth is not expected below 2000 K [3,4,6]. Fig. 4 depicts, in Row (1), the evolution of T_{seed} for Experiments (a)–(d), where T_{seed} is the temperature on the seed’s surface Σ at $(r, z) = (0, 15.8 \text{ cm} - \Delta l_c)$ (cf. Fig. 1). Comparing the evolution of T_{seed} with the $T_{seed} = 2000$ K line drawn in Row (1) of Fig. 4, one concludes that growth does not occur during the first 2 h of the heating process, and not after 3 h into the cooling process. Fig. 4 shows that the evolution of T_{seed} is virtually identical for Experiments (a)–(d). Row (2) of Fig. 4 provides information on the evolution of the temperature difference between SiC source and seed $T_{source} - T_{seed}$ for Experiments (a)–(d), where T_{source} is the temperature on the source powder’s surface at $(r, z) = (0, 14.6 \text{ cm} - \Delta l_p)$ (cf. Fig. 1). It can be seen that the initial phase is characterized by the temperature being higher at the seed than at the source. However, as required for the

growth process, $T_{source} - T_{seed}$ becomes positive well before T_{seed} becomes sufficiently large to initiate growth. The initial sign change of $T_{source} - T_{seed}$ is related to radiative heat transfer in the SiC source and in the gas phase becoming more effective with higher temperatures (cf. discussion after Eq. (11) below). Even though Fig. 4(2) shows noticeable differences between (b), (d) (for powder = 5) as compared to (a), (c) (powder = 1) (the sign change of $T_{source} - T_{seed}$ occurs some 10 min earlier for Experiments (b), (d); and Experiments (b), (d) show a spike of $T_{source} - T_{seed}$ during cooling), they should not have a significant influence on the growth process, as they occur outside the $T_{seed} > 2000$ K range.

We now proceed to analyze our numerical results with respect to the evolution of the temperature gradient both in the domain of the bulk Ω_{seed} and on the surface Σ of the SiC crystal. Due to cylindrical symmetry, the temperature gradient is completely described by its radial and by its vertical component: $\nabla T = (\partial_r T, \partial_z T)$. Therefore, in the

following, we will sometimes abuse notation and identify Ω_{seed} and Σ with their respective two-dimensional images under the projection $(r, \theta, z) \mapsto (r, z)$. As the material properties are discontinuous across the SiC seed crystal's boundary $\partial\Omega_{\text{seed}}$, ∇T can be discontinuous across $\partial\Omega_{\text{seed}}$ as well. Thus, on $\partial\Omega_{\text{seed}}$, we compute the value for ∇T on the side of Ω_{seed} , i.e. on the side of the seed crystal, and, in Ω_{seed} , we write ∇T_{seed} instead of ∇T . In detail, for $(r, z) \in \Omega_{\text{seed}}$, we compute the following approximations:

$$\nabla T_{\text{seed}}(r, z) := \left(\frac{T(r+1 \text{ mm}, z) - T(r-1 \text{ mm}, z)}{2 \text{ mm}}, \frac{T(r, z+1 \text{ mm}) - T(r, z-1 \text{ mm})}{2 \text{ mm}} \right)$$

with the following modifications on the boundary:

$$\partial_r T_{\text{seed}}(0, z) := (T(1 \text{ mm}, z) - T(0, z))/1 \text{ mm},$$

$$\partial_r T_{\text{seed}}(2 \text{ cm}, z) := (T(2 \text{ cm}, z) - T(1.9 \text{ cm}, z))/1 \text{ mm},$$

$$\partial_z T_{\text{seed}}(r, 15.8 \text{ cm} - \Delta l_c) := (T(r, 15.9 \text{ cm} - \Delta l_c) - T(r, 15.8 \text{ cm} - \Delta l_c))/1 \text{ mm},$$

$$\partial_z T_{\text{seed}}(r, 16.4 \text{ cm}) := (T(r, 16.4 \text{ cm}) - T(r, 16.3 \text{ cm}))/1 \text{ mm}.$$

On each triangle of the mesh, the values for T are computed via affine interpolation according to the values at the vertices given by the discrete solution to the finite volume scheme. Inside and within a neighborhood of the SiC crystal's domain Ω_{seed} , the grid was chosen sufficiently fine such that the diameter of each triangle was less than 1 mm.

In the bulk of the SiC crystal, defects due to thermal stress will likely be generated at locations of maximal thermal gradients, where the size of thermal gradients can be measured by the Euclidian length $|\nabla T_{\text{seed}}| := \sqrt{\partial_r T_{\text{seed}}^2 + \partial_z T_{\text{seed}}^2}$. In Row (1) of Fig. 5, we portray the evolution of the maximum norm of the temperature gradient inside Ω_{seed} , i.e. of

$$\|\nabla T_{\text{seed}}\|_{\max} := \max\{|\nabla T_{\text{seed}}(r, z)| : (r, z) \in \Omega_{\text{seed}}\}. \quad (10)$$

The precise values for six snapshots of $\|\nabla T_{\text{seed}}\|_{\max}$ are provided in Table 1. Fig. 5 also shows the location (r_{\max}, z_{\max}) where the maximum occurs, namely the r -coordinate in Row (2) and the z -coordinate in Row (3), respectively. Numerically, we determine a triangle, where $|\nabla T_{\text{seed}}(r, z)|$ is maximal, and we use the center of this triangle as (r_{\max}, z_{\max}) . Row (3) of Fig. 5 shows that, for all four experiments and throughout heating, growth, and cooling, the maximum of the temperature gradient always occurs close to the upper surface of the SiC crystal, where it is attached to the graphite crucible. From Row (2), one can see that the location of the maximum is consistently close to the vertical boundary of the crystal, except for the longest crystal lengths and during the initial cooling stage. In the latter cases, the maximum is located near the symmetry axis. Qualitatively, the maximum value of the

temperature gradient proceeds similarly for Experiments (a)–(d): it increases steadily during the initial heating process to some 10 K/cm, reaching its maximum after 3 h, i.e. at the time t_1 , where the heating power has reached its maximum (cf. Eq. (6)). The value then becomes nearly stationary at a value close to the maximum. While the crystal length increases during the growth stage, $\|\nabla T_{\text{seed}}\|_{\max}$ decreases. There is a slight increase during the initial cooling stage, but values stay well below the maximum reached during heating. The value of the maximum then decreases until, after 1.5–2.0 h of cooling, the maximum is no longer attained near the symmetry axis, but, once again, near the vertical boundary (see Row (2)). At this location, the maximum increases until $t = t_2 = 2.5$ h, which is the time, where the heating power has been reduced to zero (cf. Eq. (7)). For $t > t_2$, the maximum decays towards zero.

Quantitatively, Fig. 5, Row (1) and Table 1 display noteworthy differences between the different experiments: the maximal value of $\|\nabla T_{\text{seed}}\|_{\max}$ reached during the heating stage is some 2 K/cm lower for Experiments (c) and (d) (hole = 0) than for Experiments (a) and (b) (hole = 1), with the lowest value occurring in (c) (powder = 1, hole = 0). After $\|\nabla T_{\text{seed}}\|_{\max}$ has reached its maximum, it remains some 2–3 K/cm lower for Experiments (c) and (d) as compared to (a) and (b) throughout the remainder of the heating stage, all the growth stage, and the initial cooling stage. After 1.5 h of cooling, $\|\nabla T_{\text{seed}}\|_{\max}$ becomes almost identical for all four cases, and the order changes to (a), (c), (d), (b) (from low to high). However, as $\|\nabla T_{\text{seed}}\|_{\max}$ is overall higher during heating, the differences during the heating stage can be expected to be more significant.

Figs. 6 and 7 depict the evolution of $\nabla T_{\text{seed}}(r, z)$ for $(r, z) = (0, 15.8 \text{ cm} - \Delta l_c)$ and for $(r, z) = (1.9 \text{ cm}, 15.8 \text{ cm} - \Delta l_c)$, respectively, where the radial component is shown in the first row, the vertical component is shown in the second row, and the angle ϕ_{seed} between ∇T_{seed} and the $r = 0$ axis is shown in the third row. Moreover, the precise values for four snapshots of $\nabla T_{\text{seed}}(r, z)$ at $(r, z) = (0, 15.8 \text{ cm} - \Delta l_c)$ and at $(r, z) = (1.9 \text{ cm}, 15.8 \text{ cm} - \Delta l_c)$ are compiled in Table 2. Fig. 8 depicts the evolution of the L^2 -norm of the radial temperature gradient on the seed's surface Σ (cf. Eq. (9)), i.e. of

$$\begin{aligned} \|\partial_r T\|_{2, \Sigma} &= \sqrt{\int_{\Sigma} |\partial_r T|^2} \\ &= \sqrt{2\pi \int_0^{2 \text{ cm}} r |\partial_r T(r, 15.8 \text{ cm} - \Delta l_c)|^2 dr}. \end{aligned} \quad (11)$$

The results show some common patterns of heat field evolution present in each of the four experiments as well as differences caused by the design modifications. We will first discuss the commonalities before considering the differences. In each experiment, the heat sources are mainly concentrated close to the vertical surface of the graphite crucible in the lower part of the apparatus, due to the low

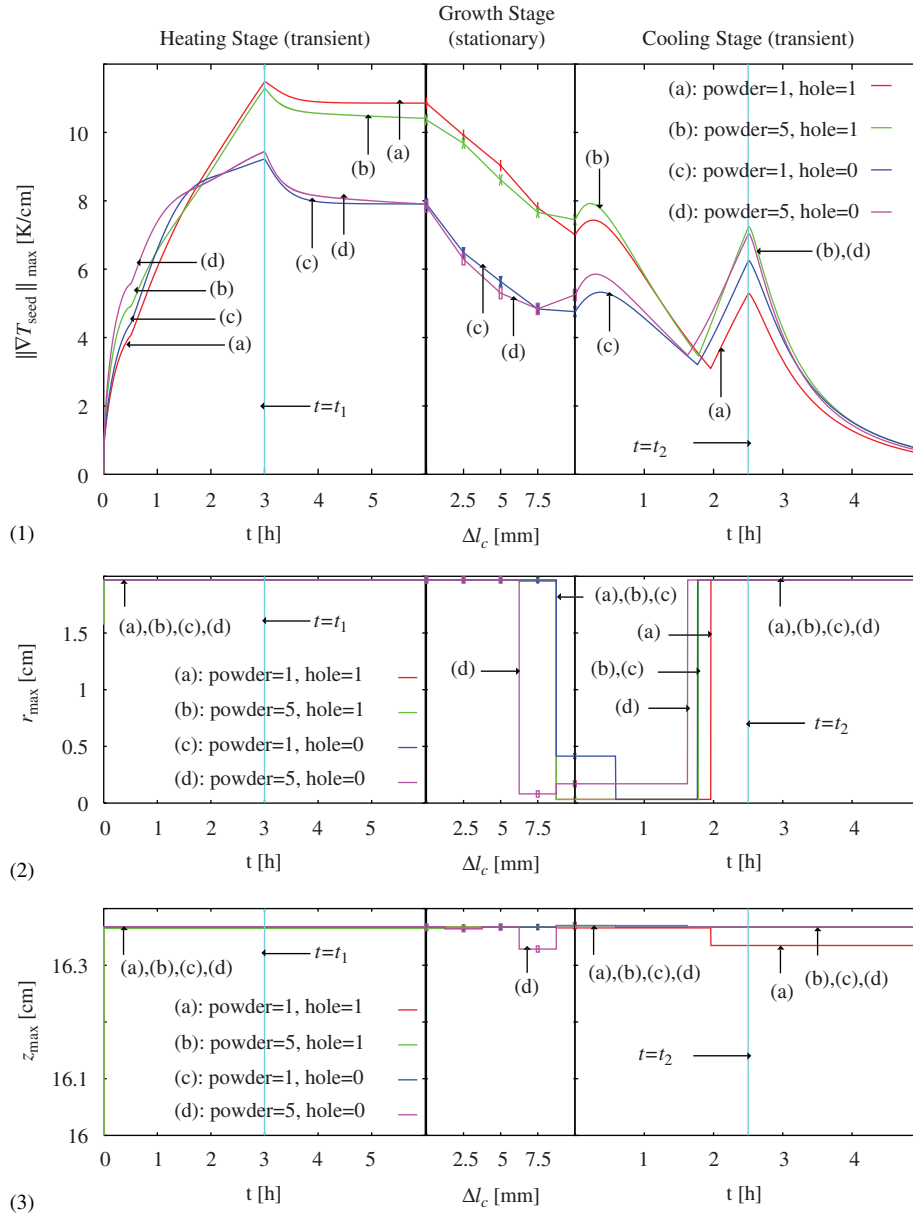


Fig. 5. Evolution of the max-norm of the length of the temperature gradient inside the SiC crystal in Row (1) together with the respective location (r_{\max} , z_{\max}), where the maximum occurs: Row (2) shows the r -coordinate and Row (3) shows the z -coordinate (see Eq. (10) and the succeeding discussion). Results of transient simulations for heating and cooling stages, results of five stationary simulations (linear interpolation in Row (1), piecewise constant interpolation in Rows (2) and (3)) for each experiment for the growth stage.

Table 1

Six snapshot values of the max-norm $\|\nabla T_{\text{seed}}\|_{\max}$ (in K/cm) of the length of the temperature gradient inside the SiC crystal for Experiments (a)–(d) (Cf. (10) and Fig. 5, Row (1))

$\ \nabla T_{\text{seed}}\ _{\max}$ (K/cm)	(a)	(b)	(c)	(d)
$t_{\text{heating}} = 3 \text{ h}$	11.5	11.3	9.2	9.4
$t_{\text{heating}} = 6 \text{ h} \approx \Delta l_c = 0$	10.9	10.4	7.9	7.9
$\Delta l_c = 5 \text{ mm}$	9.0	8.6	5.6	5.3
$t_{\text{cooling}} = 0 \equiv \Delta l_c = 10 \text{ mm}$	7.0	7.5	4.8	5.3
$t_{\text{cooling}} = 2.5 \text{ h}$	5.3	7.2	6.2	7.0
$t_{\text{cooling}} = 5 \text{ h}$	0.6	0.7	0.7	0.7

position of the induction coil rings (see Fig. 1). During the initial phase of the heating process, i.e. while the apparatus is still at low temperatures and radiation has little effect, the thermal conductivities of the SiC source powder and of the gas phase are very low as compared to those of the graphite and of the SiC seed. Thus, originating in the lower graphite part of the apparatus, upward flowing heat mainly travels *around* the SiC powder and the gas phase, reaching the SiC seed crystal from the upper right-hand graphite region above the SiC seed. This situation is reflected in Fig. 7, where both the radial and vertical components of ∇T_{seed} (1.9 cm, 15.8 cm) are shown to be increasing during

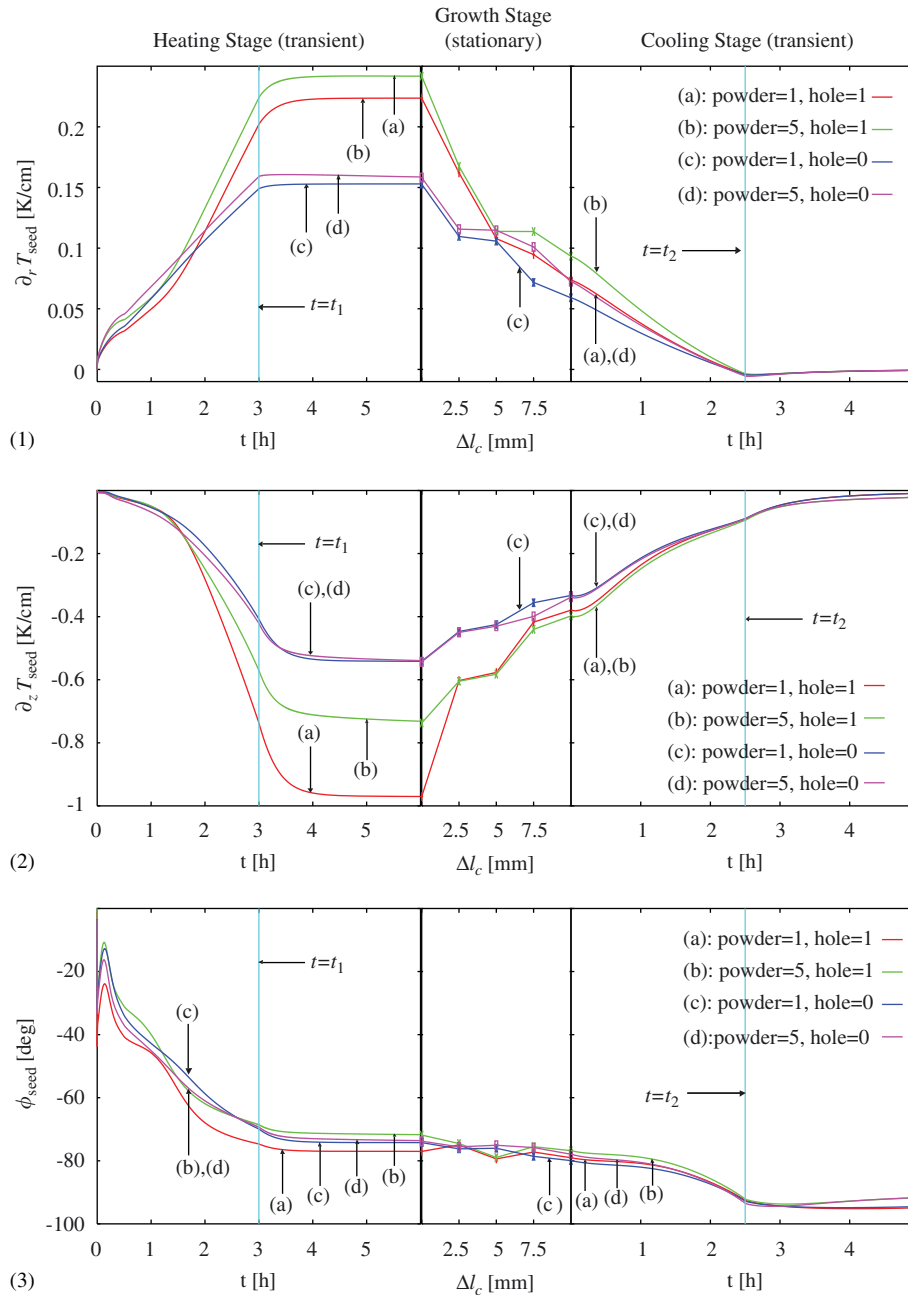


Fig. 6. Evolution of the temperature gradient $\nabla T_{\text{seed}} = (\partial_r T_{\text{seed}}, \partial_z T_{\text{seed}})$ inside the seed crystal, taken at the surface at $(r, z) = (0, 15.8 \text{ cm} - \Delta l_c)$ for Experiments (a)–(d); ϕ_{seed} is the angle between ∇T_{seed} and the $r = 0$ axis. Results of transient simulations for heating and cooling stages, results of 5 stationary simulations (linearly interpolated) for each experiment for the growth stage.

the first 1.5 h, such that ∇T_{seed} is initially pointing upward and to the right (see Fig. 7(3)). The behavior of the radial gradient $\partial_r T_{\text{seed}}$ at $(0, 15.8 \text{ cm})$ is similar (Fig. 6(1)), but the vertical gradient $\partial_z T_{\text{seed}}$ at $(0, 15.8 \text{ cm})$ is always negative. This can be explained by the insulating effect of the inner gas phase in combination with the cooling effect of the upper blind hole.

As the temperature in the apparatus continues to increase, so does the radial gradient on the seed's surface Σ (Figs. 6(1), 7(1), 8, Table 2), as the heat continues to flow from the outside to the inside of the apparatus. However,

as the radiative heat transfer through the gas phase and through the SiC powder becomes more effective, both domains become less thermally insulating, such that more and more heat reaches Σ from the gas phase, resulting in the decreasing vertical temperature gradients in Figs. 6(2) and 7(2). In particular, after some 1.5 h, $T_{\text{source}} - T_{\text{seed}}$ becomes positive (Fig. 4(2)), the source becoming warmer than the seed as is required for the growth process (cf. discussion after Eq. (9)).

While the seed temperatures established at the end of the heating process and throughout the growth stage as well as

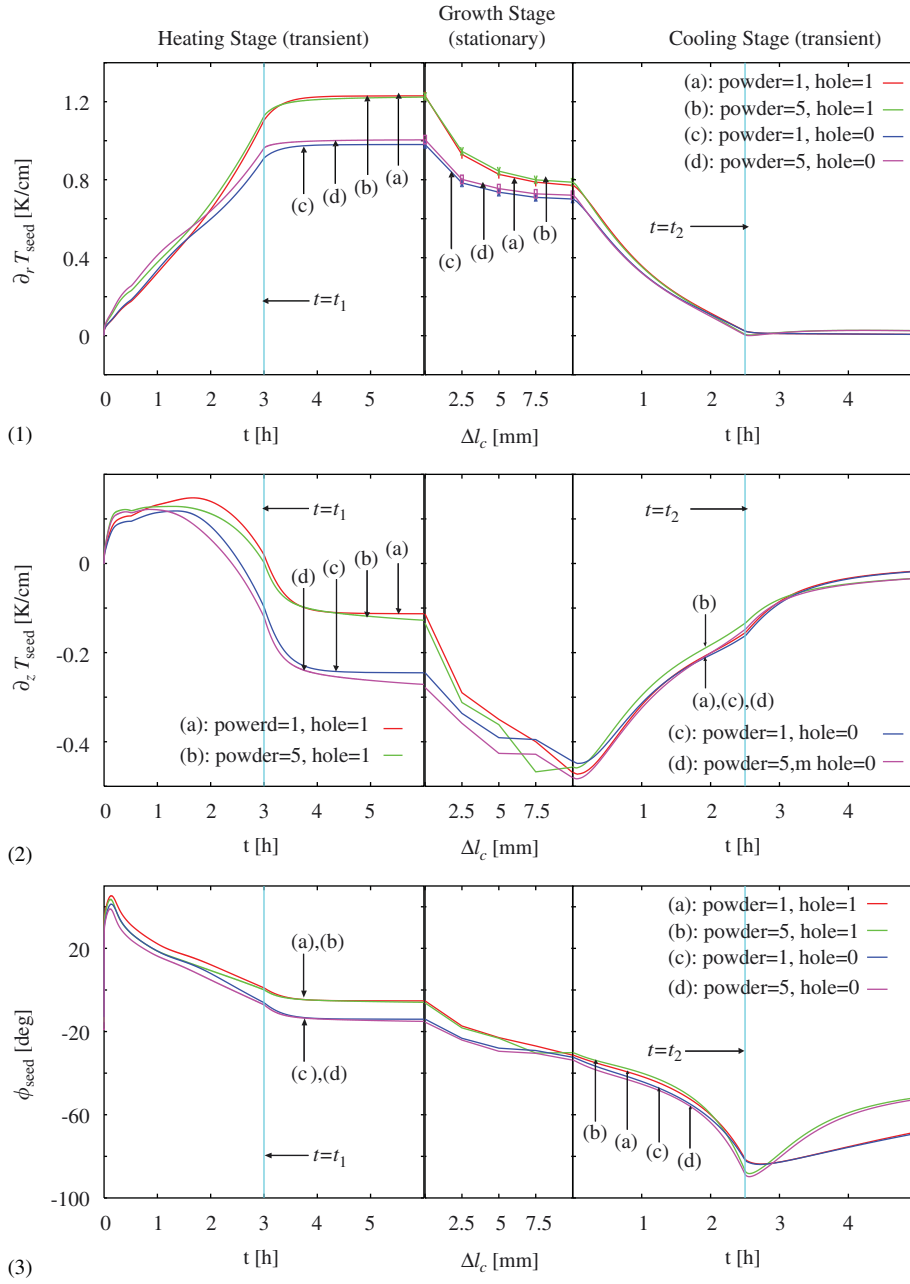


Fig. 7. Evolution of the temperature gradient $\nabla T_{\text{seed}} = (\partial_r T_{\text{seed}}, \partial_z T_{\text{seed}})$ inside the seed crystal, taken at the surface at $(r, z) = (1.9 \text{ cm}, 15.8 \text{ cm} - \Delta l_c)$ for Experiments (a)–(d); ϕ_{seed} is the angle between ∇T_{seed} and the $r = 0$ axis. Results of transient simulations for heating and cooling stages, results of 5 stationary simulations (linearly interpolated) for each experiment for the growth stage.

the qualitative evolutions of the considered temperature gradients are quite close for each of the apparatus designs (a)–(d) as discussed above, we now come to important quantitative differences in the temperature gradient evolutions. We continue to focus on ∇T_{seed} on Σ (Figs. 6 and 7, Table 2), i.e. on the temperature gradient inside the seed crystal close to the surface where growth is supposed to occur. It is reiterated that the goal is to keep ∇T_{seed} low to avoid defects due to thermal stress during growth. As explained after Eq. (9), Fig. 4(1) shows that growth does not occur during the first 2 h of the heating process. Thus, we consider $t > 2$ h in the following discussion.

Comparing Figs. 6(1), (2), 7(1), (2), and evaluating the upper part of Table 2, one finds that, at $t = 2.5$ h, the radial gradient on Σ far from the axis ($|\partial_r T_{\text{seed}}(1.9 \text{ cm}, 15.8 \text{ cm})|$, Fig. 7(1)) has the largest absolute values, namely 0.6–0.7 K/cm, while $|\partial_r T_{\text{seed}}(0, 15.8 \text{ cm})|$, $|\partial_z T_{\text{seed}}(0, 15.8 \text{ cm})|$, $|\partial_z T_{\text{seed}}(1.9 \text{ cm}, 15.8 \text{ cm})|$ are all below 0.3 K/cm. By $t = 6$ h, the values for $|\partial_r T_{\text{seed}}(1.9 \text{ cm}, 15.8 \text{ cm})|$ have increased to 0.98–1.23 K/cm. For the experiments with the smaller hole, (c), (d), the value is some 0.2 K/cm lower than for the experiments with the larger hole (a), (b). The size of the powder charge has a much smaller influence on the size of the gradient. That, at least at higher

temperatures, the size of ∇T_{seed} on Σ depends more on the size of the upper blind hole than on the size of the powder charge, can also be observed in Figs. 6(1) and (2) as well as in Table 2. In each case, the gradients are found to be smaller for the smaller blind hole, which is also confirmed in Fig. 8, where the radial gradient is integrated over the

Table 2

Four snapshot values of the temperature gradient $\nabla T_{\text{seed}} = (\partial_r T_{\text{seed}}, \partial_z T_{\text{seed}})$ inside the seed crystal, taken at the surface at $(r, z) = (0, 15.8 \text{ cm} - \Delta l_c)$ and at $(r, z) = (1.9 \text{ cm}, 15.8 \text{ cm} - \Delta l_c)$ for Experiments (a)–(d)

Exp.	(a)	(b)	(c)	(d)
$t_{\text{heating}} = 2.5 \text{ h}$				
$\partial_r T_{\text{seed}}(0, 15.8 \text{ cm})(\text{K}/\text{cm})$	0.11	0.13	0.11	0.11
$\partial_z T_{\text{seed}}(0, 15.8 \text{ cm})(\text{K}/\text{cm})$	-0.28	-0.25	-0.18	-0.21
$\partial_r T_{\text{seed}}(1.9 \text{ cm}, 15.8 \text{ cm})(\text{K}/\text{cm})$	0.65	0.68	0.60	0.64
$\partial_z T_{\text{seed}}(1.9 \text{ cm}, 15.8 \text{ cm})(\text{K}/\text{cm})$	0.14	0.11	0.08	0.05
$t_{\text{heating}} = 6 \text{ h} \approx \Delta l_c = 0$				
$\partial_r T_{\text{seed}}(0, 15.8 \text{ cm})(\text{K}/\text{cm})$	0.22	0.24	0.15	0.16
$\partial_z T_{\text{seed}}(0, 15.8 \text{ cm})(\text{K}/\text{cm})$	-0.97	-0.74	-0.54	-0.54
$\partial_r T_{\text{seed}}(1.9 \text{ cm}, 15.8 \text{ cm})(\text{K}/\text{cm})$	1.23	1.22	0.98	1.00
$\partial_z T_{\text{seed}}(1.9 \text{ cm}, 15.8 \text{ cm})(\text{K}/\text{cm})$	-0.11	-0.13	-0.25	-0.28
$\Delta l_c = 5 \text{ mm}$				
$\partial_r T_{\text{seed}}(0, 15.8 \text{ cm} - \Delta l_c)(\text{K}/\text{cm})$	0.11	0.11	0.11	0.12
$\partial_z T_{\text{seed}}(0, 15.8 \text{ cm} - \Delta l_c)(\text{K}/\text{cm})$	-0.58	-0.58	-0.43	-0.43
$\partial_r T_{\text{seed}}(1.9 \text{ cm}, 15.8 \text{ cm} - \Delta l_c)(\text{K}/\text{cm})$	0.83	0.84	0.74	0.75
$\partial_z T_{\text{seed}}(1.9 \text{ cm}, 15.8 \text{ cm} - \Delta l_c)(\text{K}/\text{cm})$	-0.35	-0.36	-0.39	-0.43
$\Delta l_c = 10 \text{ mm}$				
$\partial_r T_{\text{seed}}(0, 15.8 \text{ cm} - \Delta l_c)(\text{K}/\text{cm})$	0.07	0.09	0.06	0.07
$\partial_z T_{\text{seed}}(0, 15.8 \text{ cm} - \Delta l_c)(\text{K}/\text{cm})$	-0.38	-0.40	-0.33	-0.34
$\partial_r T_{\text{seed}}(1.9 \text{ cm}, 15.8 \text{ cm} - \Delta l_c)(\text{K}/\text{cm})$	0.77	0.79	0.70	0.72
$\partial_z T_{\text{seed}}(1.9 \text{ cm}, 15.8 \text{ cm} - \Delta l_c)(\text{K}/\text{cm})$	-0.47	-0.46	-0.44	-0.48

entire surface Σ . In each case, the smallest value is found for (c) (powder = 1, hole = 0). Since the upper blind hole is in much closer proximity to the seed crystal than to the source powder charge, during the heating process, it is not unexpected that its size has a stronger effect on the temperature gradients at Σ . The dominance of $|\partial_r T_{\text{seed}}(1.9 \text{ cm}, 15.8 \text{ cm} - \Delta l_c)|$ over the other three values remains true throughout the heating process as well as the growth stage. However, note from Fig. 6(2) and from the lower part of Table 2 that, in Experiment (a) (powder = 1, hole = 1), $|\partial_z T_{\text{seed}}(0, 15.8 \text{ cm})|$ comes close to 1 K/cm for $t > 4 \text{ h}$, thereby being significantly larger than for the other three experiments.

During the growth stage, $|\partial_r T_{\text{seed}}(1.9 \text{ cm}, 15.8 \text{ cm} - \Delta l_c)|$ decreases by some 0.45 K/cm for (a), (b) and by some 0.3 K/cm for (c), (d). However, the advantage of lower gradients for the experiments with the smaller hole, (c), (d), persists, albeit, less prominent. Figs. 6(1), (2) and 7(2) show that, during the growth stage, $|\partial_r T_{\text{seed}}(0, 15.8 \text{ cm} - \Delta l_c)|$ decrease, $|\partial_z T_{\text{seed}}(0, 15.8 \text{ cm} - \Delta l_c)|$ increase, and $|\partial_z T_{\text{seed}}(1.9 \text{ cm}, 15.8 \text{ cm} - \Delta l_c)|$ decrease, where the detailed behavior depends on the apparatus designs of Experiments (a)–(d). During all stages of the growth process as well as for all experiments, these values are at least 0.2 K/cm below $|\partial_r T_{\text{seed}}(1.9 \text{ cm}, 15.8 \text{ cm} - \Delta l_c)|$. During the cooling stage, growth diminishes, and ∇T_{seed} on Σ is less significant, especially, as Figs. 6(1), (2) and 7(1),(2) show that ∇T_{seed} on Σ continues to decrease in all cases, remaining at least an order of magnitude below $\|\nabla T_{\text{seed}}\|_{\text{max}}$ (cf. Fig. 5).

Summarizing the above findings, we note that, for $t > 2.5 \text{ h}$ and throughout the growth stage, the size of ∇T_{seed} at Σ is consistently smaller for the hole = 0 experiments (c), (d), with a slight advantage for (c), i.e. powder = 1. Moreover, we found that, in all considered cases, the maximal size of ∇T_{seed} on Σ is determined by $|\partial_r T_{\text{seed}}(1.9 \text{ cm}, 15.8 \text{ cm} - \Delta l_c)|$. This is in agreement with the results of Refs. [7,8], where the quality of as-grown

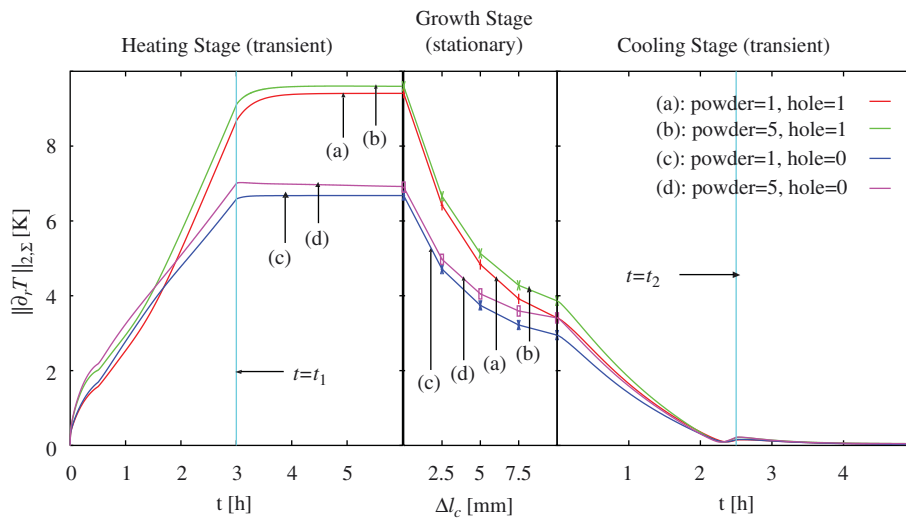


Fig. 8. Evolution of the L^2 -norm of the radial temperature gradient $\partial_r T$ on the seed's surface Σ (see Eq. (11)) for Experiments (a)–(d). Results of transient simulations for heating and cooling stages, results of five stationary simulations (linearly interpolated) for each experiment for the growth stage.

crystals was found to be improved by reducing the radial temperature gradients. However, we also point out that the radial temperature gradient on Σ was always less than 1.3 K/cm during all our simulations, and, thus, lower than the 2 K/cm that resulted in good-quality crystals according to Ref. [7].

5. Conclusions

Based on transient and stationary heat transfer models implemented in the software *WIAS-HiTNIHS*, the evolution of temperature fields was simulated for four different axisymmetric setups of PVT growth systems, varying the size of the upper blind hole and the amount of the source powder charge. Transient simulations of the heating and cooling stages were complemented by stationary simulations of the growth stage. The temperature gradients were monitored in the bulk and on the growth surface of the SiC seed crystal, where they are closely related to the quality of the as-grown crystal. In the bulk, the maximum of the temperature gradient was always established after some 3 h into the heating process at some 10 K/cm, decreasing during the growth stage, and remaining lower during cooling. The maximal temperature gradient in the bulk was always found close to the upper surface of the SiC crystal, where it is attached to the graphite crucible. For the experiments with the smaller blind hole, the maximal value of the temperature gradient in the bulk was some 2 K/cm smaller throughout the later heating stage, all the growth stage, and the initial cooling stage. The temperature gradients on the seed's growth surface were also found to increase with time and temperature during heating, then to decrease during growth and cooling. Their maximal size was determined by the radial gradients far from the symmetry axis. These gradients were some 0.3 K/cm smaller for the smaller blind hole. The size of the gradients was found to depend much less on the size of the powder charge, but being slightly smaller for the smaller amount of source powder. The seed temperature established at the end of the heating process and throughout the growth stage did not vary significantly with the considered different designs. This fact is especially noteworthy in the light of Ref. [14], where temperature-constrained stationary numerical optimizations showed that low radial temperature gradients can be achieved by reducing the crystal's temperature. However, as the growth process requires one to keep the seed crystal above a certain temperature, adjusting the size of the upper blind hole can furnish a useful alternative for further reduction of the radial temperature gradients.

Acknowledgments

This work has been supported by the Institute for Mathematics and its Applications (IMA) in Minneapolis, by the DFG Research Center MATHEON—“Mathematics for key technologies” (FZT 86) in Berlin, and by Corning

Incorporated, Corning, NY. We thankfully acknowledge the referee's helpful suggestions and advise.

References

- [1] R. Madar, J. Camassel, E. Blanquet (Eds.), Silicon Carbide and Related Materials ICSCRM, Lyon, France, vol. 457–460, October 5–10, 2003, Part II of Mater. Sci. Forum, vol. 457–460, Trans Tech Publications Ltd, 2004. (Chapters 9–11).
- [2] H.McD. Hobgood, M.F. Brady, M.R. Calus, J.R. Jenny, R.T. Leonard, D.P. Malta, St.G. Müller, A.R. Powell, V.F. Tsvetkov, R.C. Glass, C.H. Carter Jr., Mater. Sci. Forum 457–460 (2004) 3–8 Proceedings of the 10th International Conference on Silicon Carbide and Related Materials, October 5–10, 2003, Lyon, France.
- [3] Yu.M. Tairov, V.F. Tsvetkov, J. Crystal Growth 43 (1978) 209.
- [4] A.O. Konstantinov, Sublimation growth of SiC, in: G.L. Harris (Ed.), Properties of Silicon Carbide, EMIS Database Series, vol. 13, Institution of Electrical Engineers, INSPEC, London, UK, 1995, p. 170.
- [5] M. Pons, M. Anikin, K. Chourou, J.M. Dedulle, R. Madar, E. Blanquet, A. Pisch, C. Bernard, P. Grosse, C. Faure, G. Basset, Y. Grange, Mater. Sci. Eng. B 61–62 (1999) 18.
- [6] D. Schulz, M. Lechner, H.-J. Rost, D. Siche, J. Wollweber, Mater. Sci. Forum 433–436 (2003) 17–20 Proceedings of the Fourth European Conference on Silicon Carbide and Related Materials, September 2–5, 2002, Linköping, Sweden.
- [7] C.M. Balkas, A.A. Maltsev, M.D. Roth, V.D. Heydemann, M. Sharma, N.K. Yushin, Mater. Sci. Forum 389–393 (2002) 59–62 Proceedings of the Ninth International Conference on Silicon Carbide and Related Materials, October 27–November 2, 2001, Tsukuba, Japan.
- [8] S. Wang, E.M. Sanchez, A. Kopec, S. Poplawski, R. Ware, S. Holmes, C.M. Balkas, A.G. Timmerman, Mater. Sci. Forum 389–393 (2002) 35–38 Proceedings of the Ninth International Conference on Silicon Carbide and Related Materials, October 27–November 2, 2001, Tsukuba, Japan.
- [9] S.I. Nishizawa, T. Kato, Y. Kitou, N. Oyanagi, F. Hirose, H. Yamaguchi, W. Bahng, K. Arai, Mater. Sci. Forum 457–460 (2004) 29.
- [10] S.Yu. Karpov, A.V. Kulik, I.A. Zhmakin, Yu.N. Makarov, E.N. Mokhov, M.G. Ramm, M.S. Ramm, A.D. Roenkov, Yu.A. Vodakov, J. Crystal Growth 211 (2000) 347.
- [11] R. Ma, H. Zhang, V. Prasad, M. Dudley, Cryst. Growth Des. 2 (3) (2002) 213.
- [12] O. Klein, P. Philip, J. Sprekels, Interfaces Free Boundaries 6 (2004) 295.
- [13] J. Meziere, M. Pons, L. Di Cioccio, E. Blanquet, P. Ferret, J.M. Dedulle, F. Baillet, E. Pernot, M. Anikin, R. Madar, T. Billon, J. Phys. Condens. Matter 16 (2004) S1579.
- [14] C. Meyer, P. Philip, Cryst. Growth Des. 5 (3) (2005) 1145.
- [15] P. Philip, Transient numerical simulation of sublimation growth of SiC bulk single crystals. Modeling, finite volume method, results, Ph.D. Thesis, Department of Mathematics, Humboldt University of Berlin, Germany, 2003. Report No. 22, Weierstrass Institute for Applied Analysis and Stochastics (WIAS), Berlin, available at (http://www.wias-berlin.de/publications/reports/22/wias_reports_22.pdf).
- [16] O. Klein, P. Philip, J. Sprekels, K. Wilmański, J. Crystal Growth 222 (4) (2001) 832.
- [17] O. Klein, P. Philip, IEEE Trans. Magn. 38 (3) (2002) 1519.
- [18] O. Klein, P. Philip, Math. Models Methods Appl. Sci. 15 (2) (2005) 227.
- [19] J. Geiser, O. Klein, P. Philip, Numerical simulation of heat transfer in materials with anisotropic thermal conductivity: A finite volume scheme to handle complex geometries, Preprint No. 2046, Institute for Mathematics and its Applications (IMA), Minneapolis, 2005; Preprint No. 1033, Weierstrass Institute for Applied Analysis and

- Stochastics (WIAS), Berlin, 2005, submitted for publication. Available at (<http://www.ima.umn.edu/preprints/may2005/2046.pdf>).
- [20] J. Geiser, O. Klein, P. Philip, WIAS-HiTNIHS: Software-tool for simulation in sublimation growth for SiC single crystal: application and methods, in: Proceedings of the International Congress of Nanotechnology, San Francisco, November 7–10, 2004. Available at (<http://www.ianano.org/Proceeding/Geiser.pdf>).
- [21] F. Dupret, P. Nicodème, Y. Ryckmans, P. Wouters, M.J. Crochet, *Int. J. Heat Mass Transfer* 33 (9) (1990) 1849.
- [22] J. Fuhrmann, T. Koprucki, H. Langmach in: W. Hackbusch, G. Wittum (Eds.), Proceedings of the 14th GAMM Seminar on Concepts of Numerical Software, Kiel, January 23–25, 1998, University of Kiel, Kiel, Germany, 2001.
- [23] J. Shewchuk, in: First Workshop on Applied Computational Geometry, Philadelphia, Pennsylvania, ACM, 1996, p. 124.
- [24] O. Schenk, K. Gärtner, W. Fichtner, *Behav. Inf. Technol.* 40 (1) (2000) 158.
- [25] O. Schenk, K. Gärtner, J. Future Gener. Comput. Syst. 20 (3) (2004) 475.
- [26] O. Klein, P. Philip, *J. Crystal Growth* 247 (1–2) (2003) 219.
- [27] O. Klein, P. Philip, *J. Crystal Growth* 249 (3–4) (2003) 514.